Eur. Phys. J. D **28**, 67–77 (2004)
DOI: 10.1140/epjd/e2003-00295-1

THE EUROPEAN PHYSICAL JOURNAL D

Quantitative determination of the 3D dipole orientation of single molecules

A. Débarre[1,a], R. Jaffiol[1], C. Julien[1], D. Nutarelli[1], A. Richard[1], P. Tchénio[1], F. Chaput[2], and J.-P. Boilot[2]

[1] Laboratoire Aimé Cotton, UPR 3321 du CNRS, bâtiment 505, Campus d'Orsay, 91405 Orsay Cedex, France
[2] Groupe de Chimie du Solide, Physique de la Matière Condensée, UMR 7643 du CNRS, École Polytechnique, 91128 Palaiseau Cedex, France

Received 16 May 2003 / Received in final form 22 July 2003
Published online 2nd December 2003 –

Abstract. Recently, different approaches have been implemented to detect single molecules with an optical dipole out of the sample plane. Principles to solve this problem of general interest have been laid but no detailed analysis has been performed to date. This paper is devoted to a quantitative analysis of the dipole orientation of out of plane molecules that we have detected by amplitude and phase masking of the input beam. The accuracy of the orientation is discussed.

PACS. 32.50.+d Fluorescence, phosphorescence (including quenching)

1 Introduction

Efficient excitation of molecules or more generally nanoobjects with z-absorbing optical dipole oriented perpendicularly to the sample plane is an important challenge. In fact, in many anisotropic systems, like interfaces, membranes, nanoelectronic multi-layer systems, this orientation that coincides with a symmetry axis plays a fundamental role and gives complementary information to that obtained with in-plane molecules. Single-molecule spectroscopy (SMS) gives an unique opportunity to analyze at the molecular level a large number of chemical, photophysical or biological processes [1,2]. In biological applications for example, SMS can be used to analyse rotational dynamics as well as to derive dynamic distance and conformation measurements without the problem of synchronization of the processes that occurs at the multimolecular level [3]. Symmetrically, efficient and accurate determination of the orientation of the dipole of molecules is an important topic.

Since the signal comes from a single molecule emission, this powerful spectroscopic tool requires to optimise the signal-to-noise ratio (SNR). Standard single-molecule polarisation microscopy fully meets this requirement when the optical (absorption) dipole lies in the sample plane [1,4,5]. But the SNR is low when the molecule dipole is close to the normal of the sample. Efficient excitation and detection of off-plane molecules play also an important role in the context of apertureless optical near-field microscopy [6,7]. This promising technique can largely improve near-field optical spectroscopy resolution down to 20 nm [8] and could be compatible with single-molecule imaging [9]. The first out-of-plane single molecule detection was obtained by near-field optics [10]. In SNOM schemes for which the field is produced at the end of a coated tapered fibre, the field below the coating presents a non negligible z-component. When the tip is scanned over a sample doped with molecules, an efficient excitation of off-plane molecules occurs below the coated part of the aperture. As a result off-plane molecules present a specific pattern of fluorescence similar to a doughnut. This has been clearly evidenced by the group of van Hulst [11].

The opportunity of detecting out-of-plane molecules was extended into far field using large angle illumination by Trautman and Macklin in 1995 [1]. Since this demonstration, several works have been reported on this issue. Most of these approaches use amplitude masking in order to eliminate parts of the beam that have no or weak z-component. It is the case for example of the total internal reflection illumination scheme or of some related schemes combining annular illumination and the vicinity to an air/sample interface [12–16]. These schemes succeed in efficiently exciting the out-of-plane molecules provided that the probed molecules lie close to an interface at the wavelength scale. In fact, the interface plays a major role since it increases the relative weight of the z-component of the field with respect to the in-plane component [17]. Another scheme has been recently proposed, which suggests to determine the dipole orientation from the measurements of three detectors that are sensitive to different polarisations of light. This method, which has not been experimentally demonstrated, should reduce the data acquisition time assuming that noise is low [18].

Recently, we have proposed a scheme that adds phase masking of the input laser beam to amplitude masking. This scheme proved to be efficient both to excite and

[a] e-mail: anne.debarre@lac.u-psud.fr

detect out-of-plane single molecules. This procedure allowed us to obtain a large z-component of the excitation field [19]. Sometimes later, a completely radially-polarised light was implemented. Then, the amplitude of the z-component of the field is optimised [20]. At the same time, Hell proposed another scheme based on engineering of the point-spread function in confocal microscopy [21]. The basic idea of all methods relies on the observation that for a classical excitation through a high numerical aperture objective, the z-components of the fields of the different rays interfere destructively on the optical axis of the microscope in the focal plane. These components are rejected into lateral lobes. The consequence is that the volume of excitation of out-of-plane molecules is off-axis. As a result their fluorescence cannot be efficiently collected in a confocal scheme. It thus implies that SNR for detection is low. Detection of off-plane molecules in classical polarisation schemes requires clear samples without scattering. If beam shaping is involved, the roles of the in-plane and z-components can be reversed, which implies both efficient excitation and collection of the fluorescence of out-of-plane molecules. Up to now, papers have laid the basic principles of calculation of the field patterns at the focus plane with respect to the polarisation state of the exciting field. In order to derive the ability of such schemes to be useful tools to follow the dynamics of dipole reorientation, a detailed calculation of field patterns and fluorescence patterns with respect to a given amplitude and/or phase masking scheme is needed. This is one aim of the present paper. Its final aim is to determine to which extend such a scheme can be useful to derive quantitatively the orientation of the molecular dipole. In a first part of the paper we recall the basic principles of the calculation of the field at the focal plane, then we derive the complete expression of the field, including the effect of the interface relative to the presence of the sample substrate. This expression of the field is explicitly derived for a particular masking configuration but it can be readily extended to different configurations of beam shaping either by amplitude or by phase masking. We then derive the expression of the intensity of the fluorescence emitted by a molecule of given dipolar orientation. In a second part of the paper, the experimental set-up is recalled and examples of recorded fluorescence patterns of single molecules are reported. Finally in a third part, an image correlation algorithm is used to compare the resulting experimental patterns with the calculated ones. It allows us to derive quantitatively the dipolar orientation of the recorded molecules. The accuracy of the orientation is discussed.

2 Calculation of the excitation field pattern in the focal plane

2.1 Basic principles of the polarisation schemes

The amplitude, phase and polarisation of the excitation beam is usually "quasi geometrically" prepared by optical elements before the entrance pupil of the objective. Quasi-geometrically means that evanescent waves and aperture fields play a minor role. After the exit pupil, the phase, the amplitude and the polarisation of the prepared beam determine beam focusing and polarisation properties in the focal plane by free propagation in a quasi-homogeneous medium. As demonstrated long ago by Richards and Wolf, free propagation is exactly described in the frame of plane-wave decomposition [22]. This last principle allows one to calculate the diffraction pattern in the focal plane of the microscope, even for very large numerical aperture objectives. Following the notations of Richards and Wolf, the field in the focal plane of the quasi-homogeneous medium writes as:

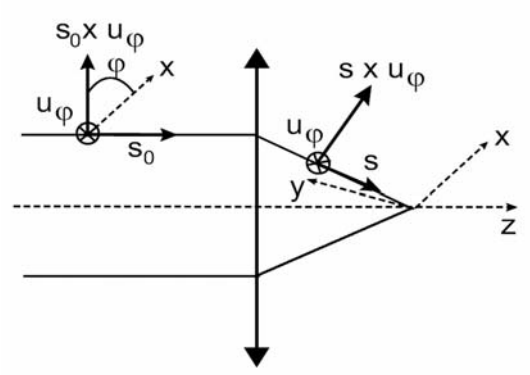

Fig. 1. Schematics of the frame used for the calculation of the components of the excitation field $\overrightarrow{E}$.

$$\overrightarrow{e}\,(x,y,z) = \frac{-ik}{2\pi}\iint d\Omega\ \overrightarrow{a}\,(s_x,s_y)\ \ e^{ik(s_x x+s_y y+s_z z)} \tag{1}$$

$d\Omega$ is the solid angle corresponding to the rays emerging from the optical system. $\overrightarrow{a}$ is the strength of the electric field that is incident on the exit pupil. It corresponds to the prepared field. $\overrightarrow{s}$ is a unit vector along the relevant ray and directed towards the exit of the optical system. k is equal to $2n\pi/\lambda$, where n is the refractive index of the propagation medium and λ the excitation wavelength in vacuum.

In the present calculation, we assume that the objective is aplanetic. In a frame defined by the unit vectors $\overrightarrow{s}$ of the ray, $\overrightarrow{u_\varphi}$ perpendicular to $\overrightarrow{s}$ and to the plane defined by the ray and the optical axis of the system (meridian plane) and by $\overrightarrow{u_\theta} = \overrightarrow{s} \times \overrightarrow{u_\varphi}$ (Fig. 1), $\overrightarrow{a}\,(s_x,s_y)$ expresses as:

$$\overrightarrow{a}\,(s_x,s_y) = Af\cos^{1/2}(\theta)\,[(\overrightarrow{e}_0\cdot\overrightarrow{u}_\varphi)\,\overrightarrow{u}_\varphi + (\overrightarrow{e}_0\cdot(\overrightarrow{s}_0\times\overrightarrow{u}_\varphi))\,(\overrightarrow{s}\times\overrightarrow{u}_\varphi)]\,. \tag{2}$$

In this expression $\overrightarrow{e_0}$ is the polarisation vector of the incident field in the entrance pupil. θ is the tilt of the ray with respect to the optical axis. f is the focal length of the objective. A is the amplitude of the incident light. This relation expresses that the angle between the polarisation and the meridian plane remains constant when the light traverses the objective. Note that the vector $\overrightarrow{s} \times \overrightarrow{u_\varphi}$ is

identical to the "$\overrightarrow{g_1}$" vector introduced by Richards and Wolf.

Generally, high numerical aperture objectives imply propagation of the beam in a high refractive index medium after the exit pupil of the objective. In single molecule polarisation microscopy, the sample itself is composed of a very thin film deposited on a glass cover plate or substrate, which refractive index matches that of the propagative medium at the exit pupil of the objective. The excitation of the molecules located in the thin film generally implies to cross the high index contrast interface between the sample substrate and the sample itself. As a result, we extend the general formalism introduced by Richards and Wolf to include the effect of the interface. A pioneer work on the effects of a plane interface on the refraction properties of an electromagnetic wave has been performed by the group of Stamnes [23]. The focusing properties of light after a planar interface has been discussed by Török et al. [24]. In order to derive the field strength $\overrightarrow{a}'$ after the interface, we need to calculate the expression of electric field $\overrightarrow{e}'$ after the interface.

2.2 Calculation of the field strength in the focal plane after crossing an interface

The components of the transmitted and reflected fields after the crossing of the interface are determined by Descartes' law, which expresses the conservation of the vector $\vec{K}$ for the wavevectors of the incident ($i = 1$), transmitted reflected ($i = 2$) and reflected fields ($i = 3$):

$$\overrightarrow{K} = \overrightarrow{k_i} \times \overrightarrow{n_i} \quad i = 1, 2, 3 \tag{3}$$

$\vec{n}$ is the unit vector normal to the interface. $\vec{n}$ and $\overrightarrow{s}$ determine the incident plane at the interface. In the present situation, we consider the case where the ray emerges from a medium of index n to focus at the interface in the air. Then $\overrightarrow{a}$ becomes $\overrightarrow{a}'$:

$$\overrightarrow{a}'(s_x, s_y) = Af\cos^{1/2}(\theta)\left[\frac{2k_{1z}}{k_{1z}+k_{2z}}(\overrightarrow{e}_0 \cdot \overrightarrow{u}_\varphi)\ \overrightarrow{u}_\varphi\right] + Af\cos^{1/2}(\theta)\left[\frac{2\,n^2 k_{1z}}{k_{1z}+n^2 k_{2z}} \times (\overrightarrow{e}_0 \cdot (\overrightarrow{s}_0 \times \overrightarrow{u}_\varphi))\,(\overrightarrow{s}' \times \overrightarrow{u}_\varphi)\right] \tag{4}$$

where $\overrightarrow{s}' = \overrightarrow{k}_2/k_1$. The wavevectors express as follows:

$$\overrightarrow{k}_1 = \overrightarrow{k}_{1T} + \overrightarrow{k_{1z}} = \frac{n\omega}{c}\overrightarrow{s}$$
$$\overrightarrow{k}_2 = \overrightarrow{k}_{1T} + \frac{\sqrt{1-n^2\sin^2\theta}}{n\cos\theta}\overrightarrow{k}_{1z}.$$

In equation (4), the first term corresponds to the component of polarisation perpendicular to the incidence plane (s-polarisation) and the second term to the component of polarisation in the incidence plane (p-polarisation). It is convenient to introduce the polar coordinates r, θ and φ, with the polar axis $\theta = 0$ in the z-direction to express $\overrightarrow{a}'(s_x, s_y)$:

$$\overrightarrow{a}'(s_x, s_y) = Af\cos^{1/2}(\theta)\left[\frac{2n\cos\theta}{n\cos\theta+\sqrt{1-n^2\sin^2\theta}}(\overrightarrow{e}_0 \cdot \overrightarrow{u}_\varphi)\,\overrightarrow{u_\varphi}\right] + Af\cos^{1/2}(\theta)\left[\frac{2n^2\cos\theta}{\cos\theta+n\sqrt{1-n^2\sin^2\theta}} \times (\overrightarrow{e}_0 \cdot (\overrightarrow{s}_0 \times \overrightarrow{u}_\varphi))\ (\overrightarrow{s}' \times \overrightarrow{u}_\varphi)\right] \tag{5}$$

with:

$$\overrightarrow{u_\varphi} = \begin{pmatrix}\sin\varphi\\ -\cos\varphi\\ 0\end{pmatrix}, \quad (\overrightarrow{s}_0 \times \overrightarrow{u}_\varphi) = \begin{pmatrix}\cos\varphi\\ \sin\varphi\\ 0\end{pmatrix}$$

$$\text{and } (\overrightarrow{s}' \times \overrightarrow{u}_\varphi) = \frac{1}{n}\begin{pmatrix}\cos\varphi\sqrt{1-n^2\sin^2\theta}\\ \sin\varphi\sqrt{1-n^2\sin^2\theta}\\ -n\sin\theta\end{pmatrix}$$

φ is the angle between x-axis and vector $\overrightarrow{s}_0 \times \overrightarrow{u}_\varphi$. Finally the electric field focusing just after the interface reads as:

$$\overrightarrow{e}'(x, y, z) = \frac{-ik}{2\pi}\iint d\Omega\,\overrightarrow{a}'(s_x, s_y) \times e^{i\frac{2\pi}{\lambda}\left(n\sin\theta\cos\varphi\ x + n\sin\theta\sin\varphi\ y + \sqrt{1-n^2\sin^2\theta^2}z\right)} \tag{6}$$

where $d\Omega = \sin\theta d\theta d\varphi$. Equations (5, 6) are very general. In fact, one can calculate the pattern of the focusing field in any configuration of polarisation, phase and amplitude shaping of the excitation beam, given the expression of the corresponding incident field $\overrightarrow{e}_0$. In the more general case $\overrightarrow{e}_0$ can be expressed as the product of a tensorial matrix of transmission $\bar{t}$ that takes into account the phase and the amplitude by the polarisation of the initial excitation field.

Let us first assume that the initial polarisation of the excitation field is linear and oriented along the x-direction and that no masking is implemented in the entrance pupil, then $\overrightarrow{e}_0 = (1, 0, 0)$ and equation (5) becomes:

$$\overrightarrow{a}'(\theta, \varphi) = Af\cos^{1/2}\theta\sin\varphi\frac{2n\cos\theta}{n\cos\theta+\sqrt{1-n^2\sin^2\theta}}\begin{pmatrix}\sin\varphi\\ -\cos\varphi\\ 0\end{pmatrix} + Af\cos^{1/2}\theta\cos\varphi\frac{2n\cos\theta}{\cos\theta+n\sqrt{1-n^2\sin^2\theta}} \times \begin{pmatrix}\cos\varphi\sqrt{1-n^2\sin^2\theta}\\ \sin\varphi\sqrt{1-n^2\sin^2\theta}\\ -n\sin\theta\end{pmatrix}. \tag{7}$$

If we consider the symmetry of revolution of the microscope, it is convenient to introduce the (ϱ, ψ) coordinates of a point in the focal plane, defined as follows:

$$\frac{n\omega}{c}x = \varrho\cos\psi, \frac{n\omega}{c}y = \varrho\sin\psi \quad \text{with} \quad \varrho = \frac{n\omega}{c}\sqrt{x^2+y^2}.$$

The components of the field in the focal plane are obtained in a straightforward calculation as:

$$\begin{aligned}
e'_x(\varrho,\psi) &= -\frac{ikAf}{2\pi}\int_0^{\theta_M} \sin\theta\cos^{1/2}\theta K_2(\theta) \\
&\quad \times [J_0(\varrho\sin\theta) + \cos(2\psi)J_2(\varrho\sin\theta)]\, d\theta \\
&\quad - \frac{ikAf}{2\pi}\int_0^{\theta_M} \sin\theta\cos^{1/2}\theta K_1(\theta) \\
&\quad \times [J_0(\varrho\sin\theta) - \cos(2\psi)J_2(\varrho\sin\theta)]\, d\theta \\
e'_y(\varrho,\psi) &= \frac{ikAf}{2\pi}\ \sin(2\psi)\int_0^{\theta_M} \sin\theta\cos^{1/2}\theta \\
&\quad \times [K_1(\theta) - K_2(\theta)]\ \ J_2(\varrho\sin\theta)d\theta \\
e'_z(\varrho,\psi) &= -\frac{kAf}{2\pi}\ \cos\psi\int_0^{\theta_M} 2\sin^2\theta\cos^{1/2}\theta \\
&\quad \times \frac{nK_1(\theta)}{\sqrt{1-n^2\sin^2\theta}}\ J_1(\varrho\sin\theta)d\theta
\end{aligned} \tag{8}$$

where,

$$\begin{aligned}
J_0(\varrho\sin\theta) &= \frac{1}{2\pi}\int_0^{2\pi} e^{i\varrho\sin\theta\cos(\varphi-\psi)}d\varphi \\
J_1(\varrho\sin\theta)\cos\psi &= \frac{1}{2\pi i}\int_0^{2\pi} \cos\varphi e^{i\varrho\sin\theta\cos(\varphi-\psi)}d\varphi \\
J_2(\varrho\sin\theta)\sin(2\psi) &= -\frac{1}{2\pi}\int_0^{2\pi} \sin(2\varphi)e^{i\varrho\sin\theta\cos(\varphi-\psi)}d\varphi
\end{aligned} \tag{9}$$

and,

$$\begin{aligned}
K_1(\theta) &= \frac{2\pi n\cos\theta\sqrt{1-n^2\sin^2\theta}}{\cos\theta + n\sqrt{1-n^2\sin^2\theta}} \\
K_2(\theta) &= \frac{2\pi n\cos\theta}{n\cos\theta + \sqrt{1-n^2\sin^2\theta}}
\end{aligned}$$

$n\sin\theta_M = NA$. NA is the numerical aperture of the objective. The rays for which $NA > 1$ give rise to evanescent waves after the interface, but they do contribute to the sample excitation. In Cartesian coordinates, these components express as follows:

$$\begin{aligned}
e'_x(x,y,0) &= -\frac{ikAf}{2\pi}\int_0^{\theta_M} \sin\theta\cos^{1/2}\theta K_2(\theta) \\
&\quad \times \left[J_0\left(\frac{n\omega}{c}\sqrt{x^2+y^2}\sin\theta\right)\right. \\
&\quad \left. + \frac{x^2-y^2}{x^2+y^2}J_2\left(\frac{n\omega}{c}\sqrt{x^2+y^2}\sin\theta\right)\right]d\theta \\
&\quad - \frac{ikAf}{2\pi}\int_0^{\theta_M} \sin\theta\cos^{1/2}\theta K_1(\theta) \\
&\quad \times \left[J_0\left(\frac{n\omega}{c}\sqrt{x^2+y^2}\sin\theta\right)\right. \\
&\quad \left. - \frac{x^2-y^2}{x^2+y^2}J_2\left(\frac{n\omega}{c}\sqrt{x^2+y^2}\sin\theta\right)\right]d\theta \\
e'_y(x,y,0) &= \frac{ikAf}{2\pi}2\frac{xy}{x^2+y^2} \\
&\quad \times \int_0^{\theta_M} \sin\theta\cos^{1/2}\theta\,[K_1(\theta) - K_2(\theta)] \\
&\quad \times J_2(\frac{n\omega}{c}\sqrt{x^2+y^2}\sin\theta)d\theta \\
e'_z(x,y,0) &= -\frac{kAf}{2\pi}\frac{x}{\sqrt{x^2+y^2}} \\
&\quad \times \int_0^{\theta_M} 2\sin^2\theta\cos^{1/2}\theta\frac{nK_1(\theta)}{\sqrt{1-n^2\sin^2\theta}} \\
&\quad \times J_1(\frac{n\omega}{c}\sqrt{x^2+y^2}\sin\theta)d\theta.
\end{aligned} \tag{10}$$

These are the patterns that are obtained in a classical microscope, assuming that the incoming beam is linearly polarised. They are displayed in Figure 2a together with the relevant one-dimensional field intensity curves for the components $e'_x(x,0,0)$ and $e'_z(x,0,0)$ along the x-direction.

2.3 Calculation of the focal field pattern when masking

2.3.1 Amplitude masking

We first consider the currently-used circular opaque mask. The mask of radius ϱ_D is centred on the optical axis in the entrance pupil of the objective of radius ϱ_P. The revolution symmetry is preserved and equation (8) holds

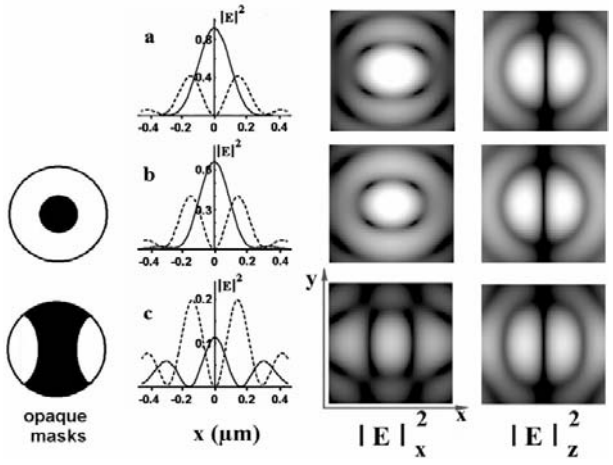

Fig. 2. Intensity patterns of the field components at the focal plane for different amplitude masks, after an interface. Left column: profile of the intensity pattern along the x-axis; $|E|_x^2$: full line, $|E|_z^2$: dashed line. Right columns: $|E|_x^2$, $|E|_z^2$ patterns at the focal plane. The excitation beam is initially linearly polarised along x. From top line to bottom line: (a) without mask, (b) with a circular opaque mask; radius ϱ_D and $\varrho_D/\varrho_P = 0.4$, ρ_p is the pupil radius (c) with a "bone-shape" opaque mask elongated in the y-direction; halfwidth Δ_D and $\Delta_D/\varrho_P = 0.4$. The absolute intensity of the profile (a) is arbitrary, but the relative intensities between the profiles for $|E|_x^2$ and $|E|_z^2$ for a given configuration (a), (b) and (c) and between two such configurations are meaningful.

with $\theta_m < \theta < \theta_M$,

$$
\begin{aligned}
e'_x(\varrho,\psi) = &-\frac{ikAf}{2\pi}\int_{\theta_m}^{\theta_M} \sin\theta\cos^{1/2}\theta K_2(\theta)\\
&\times\left[J_0(\varrho\sin\theta)+\cos(2\psi)J_2(\varrho\sin\theta)\right]d\theta\\
&-\frac{ikAf}{2\pi}\int_{\theta_m}^{\theta_M} \sin\theta\cos^{1/2}\theta K_1(\theta)\\
&\times\left[J_0(\varrho\sin\theta)-\cos(2\psi)J_2(\varrho\sin\theta)\right]d\theta
\end{aligned}
$$

$$
\begin{aligned}
e'_y(\varrho,\psi) = &\frac{ikAf}{2\pi}\ \sin(2\psi)\int_{\theta_m}^{\theta_M} \sin\theta\cos^{1/2}\theta\\
&\times\left[K_1(\theta)-K_2(\theta)\right]\ J_2(\varrho\sin\theta)\ d\theta
\end{aligned}
$$

$$
\begin{aligned}
e'_z(\varrho,\psi) = &-\frac{kAf}{2\pi}\ \cos\psi\int_{\theta_m}^{\theta_M} 2\sin^2\theta\cos^{1/2}\theta\\
&\times\frac{nK_1(\theta)}{\sqrt{1-n^2\sin^2\theta}}\ J_1(\varrho\sin\theta)\ d\theta
\end{aligned}
\qquad (11)
$$

where $\theta_m = \arcsin((\varrho_D/\varrho_P)\sin\theta_M)$.

The shape of the main lobe in the focal plane remains unchanged with respect to the case of the absence of masking but the relative weight of the z-component increases with the radius of the mask at the expense of the intensity of excitation in the focal plane. This is illustrated in Figure 2b, for the case where $\varrho_D/\varrho_P = 0.4$. In this configuration, the z-component is still concentrated into two off-optical axis lobes and the signal of a z-oriented nanoobject cannot be efficiently detected in confocal microscopy.

We then consider the case where the amplitude mask is not circular. It has a "bone-shape" (see Fig. 2c) and it is elongated in the direction perpendicular to the polarisation of the incident beam. In the above expressions, the linear polarisation was assumed to be along x and the mask is assumed to be elongated along y. This mask eliminates the rays close to the Oyz plane (z is the optical axis direction) that do not contribute to the z-component of the field. As a result it is optimised in order to get the highest possible ratio between the weights of the z-component and x-component. The revolution symmetry is no longer preserved and field components no longer express as functions of J_0, J_1 and J_2. The expression of the field can be derived from equations (6, 7),

$$
\begin{aligned}
e'_x(x,y,0) = &-2\frac{ikAf}{\pi^2}\int_{\theta_m}^{\theta_M}\int_0^{\varphi(\theta)} \sin\theta\cos^{1/2}\theta\\
&\times\left[\sin^2\varphi K_2(\theta)+\cos^2\varphi K_1(\theta)\right]\\
&\times\cos\left(\frac{n\omega}{c}x\sin\theta\cos\varphi\right)\cos\left(\frac{n\omega}{c}y\sin\theta\sin\varphi\right)d\theta d\varphi
\end{aligned}
$$

$$
\begin{aligned}
e'_y(x,y,0) = &\ 2\frac{ikAf}{\pi^2}\int_{\theta_m}^{\theta_M}\int_0^{\varphi(\theta)} \sin\theta\cos^{1/2}\theta\\
&\times\sin\varphi\cos\varphi\left[K_1(\theta)-K_2(\theta)\right]\\
&\times\sin\left(\frac{n\omega}{c}x\sin\theta\cos\varphi\right)\sin\left(\frac{n\omega}{c}y\sin\theta\sin\varphi\right)d\theta d\varphi
\end{aligned}
$$

$$
\begin{aligned}
e'_z(x,y,0) = &-2\frac{kAf}{\pi^2}\int_{\theta_m}^{\theta_M}\int_0^{\varphi(\theta)} \sin^2\theta\\
&\times\cos^{1/2}\theta\cos\varphi\frac{nK_1(\theta)}{\sqrt{1-n^2\sin^2\theta}}\\
&\times\sin\left(\frac{n\omega}{c}x\sin\theta\cos\varphi\right)\cos\left(\frac{n\omega}{c}y\sin\theta\sin\varphi\right)d\theta d\varphi
\end{aligned}
\qquad (12)
$$

θ and φ range on limited domains:

$$
\begin{aligned}
\theta_m &= \arcsin\left(\frac{\Delta_D}{\varrho_P}\sin\ \theta_M\right)\\
\varphi(\theta) &= \arccos\left(\frac{\Delta_D}{\rho_P}\frac{\sin\ \theta_M}{\sin\theta}\right)
\end{aligned}
\qquad (13)
$$

Δ_D is half the width of the elongated mask. In this situation, the field component patterns are elongated in the y-direction and the relative intensity of the z with respect to the x-components is increased. The shape of the pattern corresponds to the diffraction pattern of two "oval" slits. This leads to the observation of several lobes in the excitation patterns, which reflect the interference pattern similar to that observed for Young slits. It also leads to the elongation of the lobes in the y-direction, because each slit has a height smaller than the diameter of the pupil. The asymmetry of the lobes increases with the width of mask, but so does the relative weight of the z-component. The component patterns are displayed in Figure 2c for the case where $\Delta_D/\varrho_P = 0.4$. The width of the elongated

mask is chosen equal to the diameter of the circular mask. In this situation, the ratio between the y-dimension and the x-dimension is of the order of 1.5 and the ratio of the z-component to the x-component is 1.8. The size of the mask has been chosen in order to have a satisfying compromise between the value of the remaining excitation energy and of the weight of the z-component. The relative weight of the z-component without masking, with a circular mask and with an elongated mask is 0.45, 0.62 and 1.8 respectively. Nevertheless, the excitation volume of the z-component is still off-axis in this configuration.

2.3.2 Phase masking

We restrict the calculation to the mask that we have implemented to record the fluorescence pattern of single molecules. Nevertheless, equation (6) allows one to derive expressions for different types of phase masks provided that a tensorial matrix is introduced in equation (5) to take into account the specific mask transmission. The experimental phase mask dephases one half of the beam by π. When the alignment is such that the dephased part corresponds to $x < 0$ (indifferently $x > 0$), then the roles of $e'_x(x, y, 0)$ and of $e'_z(x, y, 0)$ can be exchanged. The mask corresponds to a transmission function $t(\theta, \varphi)$ such that:

$$t(\theta, \varphi) = t(\theta, -\varphi) = -t(\theta, \pi - \varphi) \tag{14}$$

and the field components express as:

$$\begin{aligned}
e'_x(x, y, 0) &= 2\frac{kAf}{\pi^2} \int_{\theta_m}^{\theta_M} \int_0^{\varphi(\theta)} \sin\theta \cos^{1/2}\theta \\
&\times \left[\sin^2\varphi K_2(\theta) + \cos^2\varphi K_1(\theta)\right] \\
&\times \sin\left(\frac{n\omega}{c} x \sin\theta\cos\varphi\right) \cos\left(\frac{n\omega}{c} y \sin\theta\sin\varphi\right) d\theta d\varphi \\
e'_y(x, y, 0) &= 2\frac{kAf}{\pi^2} \int_{\theta_m}^{\theta_M} \int_0^{\varphi(\theta)} \sin\theta \cos^{1/2}\theta \\
&\times \sin\varphi\cos\varphi\left[-K_2(\theta) + K_1(\theta)\right] \\
&\times \cos\left(\frac{n\omega}{c} x \sin\theta\cos\varphi\right) \sin\left(\frac{n\omega}{c} y \sin\theta\sin\varphi\right) d\theta d\varphi \\
e'_z(x, y, 0) &= 2\frac{ikAf}{\pi^2} \int_{\theta_m}^{\theta_M} \int_0^{\varphi(\theta)} \sin^2\theta \cos^{1/2}\theta \\
&\times \cos\varphi \frac{nK_1(\theta)}{\sqrt{1 - n^2\sin^2\theta}} \\
&\times \cos\left(\frac{n\omega}{c} x \sin\theta\cos\varphi\right) \cos\left(\frac{n\omega}{c} y \sin\theta\sin\varphi\right) d\theta d\varphi
\end{aligned} \tag{15}$$

where θ_m and $\varphi(\theta)$ are given by equations (13). The case $\theta_m = 0$ and $\varphi(\theta) = \pi/2$, corresponds to phase masking only. Comparison between the expression of $e'_z(x, y, 0)$ in equations (15) and $e'_x(x, y, 0)$ in equations (12) clearly demonstrates that the role of the two components has been exchanged under masking. The $e'_z(x, y, 0)$ and $e'_x(x, y, 0)$ patterns are displayed in Figure 3 together with their intensity profile along the x-axis.

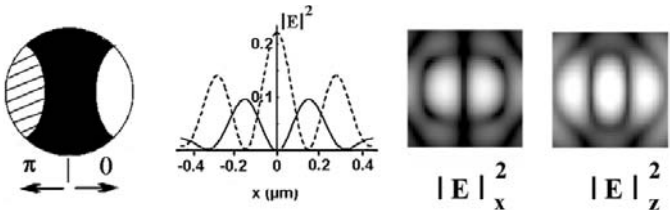

Fig. 3. Intensity patterns of the field components at the focal plane for amplitude and phase masking, after an interface. The figure corresponds to the "z" configuration of polarisation; on left side, schematics of the relevant "bone-shape" amplitude and phase masks (see text); conventions are similar to those of Figure 2.

2.4 Fluorescence excitation patterns at focal plane

Single molecules offer the opportunity of probing the characteristics of an exciting field. They can be considered as point objects and their response is sensitive both to the microscope configuration and to the structure of the incoming excitation beam. If a single molecule is excited in its absorption spectral band, it emits a fluorescence signal which is directly related to its absorption dipole orientation. Let $\vec{\mu}$ be this absorption dipole and $\vec{E}'$ the excitation beam in the focal plane where the molecule is located, then the fluorescence signal F reads as:

$$F \propto \left|\vec{\mu} \cdot \vec{E}'\right|^2 = \left|\mu_x e'_x + \mu_y e'_y + \mu_z e'_z\right|^2. \tag{16}$$

The fluorescence signal is maximum when the field polarisation and the molecular dipole are aligned. In polarisation studies in classical microscopy, the variations of the fluorescence intensity are recorded as a function of the linear polarisation orientation in the plane of the entrance pupil. The orientation for which the maximum is recorded determines the orientation of the in-plane component of the dipole of the molecule. This method is not suited to determine the off-plane component. When the incoming excitation is linearly polarised, the component e'_z is weak and the excitation of off-plane molecules is not efficient. Moreover, if confocal microscopy is used, the fluorescence detection is sensitive only for signals which are emitted when the molecule orientation is very close to the (x, y)-plane because of the inherent spatial filtering of the microscope. The detection of off-plane molecules is not efficient either. As demonstrated above, the roles of in-plane excitation and z-excitation can be exchanged by using phase masking or wave-preparation of the excitation beam. In such situations, the excitation and detection efficiency of confocal microscopy are extended to off-plane molecules. In the special cases for which the molecular dipole orientation is aligned along one of the axes, x, y or z, the excitation fluorescence pattern matches that of the corresponding excitation field component in the focal plane. The patterns of $|e'_z(x, y, 0)|^2$ obtained with amplitude and phase masking (Eqs. (15)), of $|e'_x(x, y, 0)|^2$ and of $\left|e'_y(x, y, 0)\right|^2$ obtained without any mask (Eqs. (10)) can be retrieved from Figures 6, 7 and 8, respectively (see paragraph below).

Thus theory can be directly compared to experimental results, if one gets the opportunity of recording the fluorescence excitation patterns.

3 Experimental

The principles of the experimental set-up have already been described [19]. The central element is a laser-scanning confocal microscope. The fluorescence pattern in the image plane matches the fluorescence excitation pattern provided some conditions are fulfilled. First, the spatial filtering in the collection path must be released in order to collect the signal over the entire excitation pattern, typically of the order of 1 μm^2. In order to fulfil this requirement, the signal is not collected into a fibre, which core serves as pinhole contrary to previous studies, but it is directly imaged on the 200 μm-diameter active area of an avalanche photodiode. In this configuration, the detection is no longer limited to the on-axis fluorescence signals and the remaining axial and lateral selections are sufficient to preserve a high SNR in single molecule detection. More specifically, with the objective of 1.3 numerical aperture and $\times$40 magnification, the collection efficiency is constant over a 5×5 μm^2 area. Finally, one can remark that the collection efficiency indeed varies from one molecule to the other. In fact the radiation diagram of a molecule depends on the orientation of its dipole and so does the collection efficiency. The latter remains high whatever the dipole orientation because of the aperture of the objective on the one hand and of the presence of the interface due to the sample substrate on the other hand. In fact, the interface increases the collection efficiency in a backscattering configuration. But, for a given molecule, the collection efficiency is constant whatever the excitation configuration, which allows a direct comparison between images acquired in the three different excitation configurations. It allows us to determine quantitatively the 3D dipole orientation of single molecules. The sample is a 20 nm-thick film of sol-gel doped with orange perylene molecules. For z-dipolar component excitation and detection, the incoming beam is prepared by combining amplitude masking and phase masking in the entrance pupil of the objective. The excitation beam is first linearly polarised along the x-axis. The amplitude mask is an opaque mask elongated in the y-direction. Its width corresponds nearly to 40% of the beam diameter. The width preserves a sufficient excitation intensity and it allows us to get a high contrast between the weights of the remaining x-component and of the z-component of the field. The simple phase mask that we have implemented is a transparent plate with two domains of different thickness separated by a linear edge. The thickness difference is determined in order to induce a π dephasing for one half of the beam with respect to the other half. The edge of the plate is set perpendicular to the polarisation direction of the incoming beam, and thus aligned with the y-axis. The elongated opaque mask and the plate edge are aligned. The excitation wavelength is 532 nm. In order to retrieve the 3D dipolar orientation, we perform three successive scans of the area where a single molecule is localised. The first one, in presence of the masks corresponds to the optimised "z" polarisation configuration. The two others, when the masks are removed, correspond to x- and y-polarisation configurations, respectively. In order to reduce rapid photobleaching of molecules under irradiation, the excitation power was reduced down to nearly 100 μW and the sample was maintained under a vacuum of about 5×10^{-3} Torr. The orientation of the dipole with respect to the axes is determined by the two angles θ_{mol} and φ_{mol} (Fig. 4) and the collected fluorescence signal can be written as:

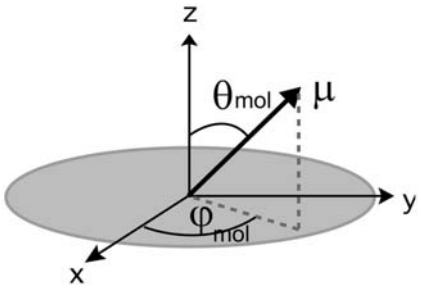

Fig. 4. Schematics of the orientation of the molecular dipole with respect to the focal plane.

$$\begin{aligned} F(x,y,0) \propto |\, & \sin(\theta_{\mathrm{mol}})\cos(\varphi_{\mathrm{mol}})e_x(x,y,0) \\ & + \sin(\theta_{\mathrm{mol}})\sin(\varphi_{\mathrm{mol}})e_y(x,y,0) \\ & + \cos(\theta_{\mathrm{mol}})e_z(x,y,0)\,|^2 \end{aligned} \tag{17}$$

$F(x,y,0)$ is the fluorescence signal produced at the point (x, y) of the focal plane when the laser is scanned in order to record a fluorescence image. Figure 5 shows three such sets of images that are obtained in the detection of three different single molecules. The acquisition time is 10 ms/pixel. The pixel number is 70 for the first image and 40 for the two others. The "visual" comparison between the fluorescence pattern of each molecule in the z-configuration and the calculated patterns of Figure 8 indicates that none of these molecules lies in the sample plane. Since the detection of in-plane molecules is covered by well-known polarisation methods, the challenge has moved over the last years towards efficient detection of out-of-plane molecules. We have thus restricted our analyse to the 3D orientation of these three molecules because they are typical examples of out-of-plane molecules. The molecule 1 presents two symmetrical lateral lobes in the y-polarisation configuration. The dipole of this molecule is thus included in the xOz plane. Its off-centre main spot in the z-configuration together with its bi-lobe pattern in the x-configuration indicate that its dipole is out of sample plane. The dipole of the molecule 2 is also off-axis. The comparison between the images in x- and y-configurations indicates that the in-plane component of its dipole is closer to the x-axis than to the y one. The molecule 3 displays a bright elongated central spot in the z-configuration and two lateral lobes in both the x- and y-configurations. The dipole of this molecule is nearly aligned with the optical axis. Beyond this estimation, the question is to know if

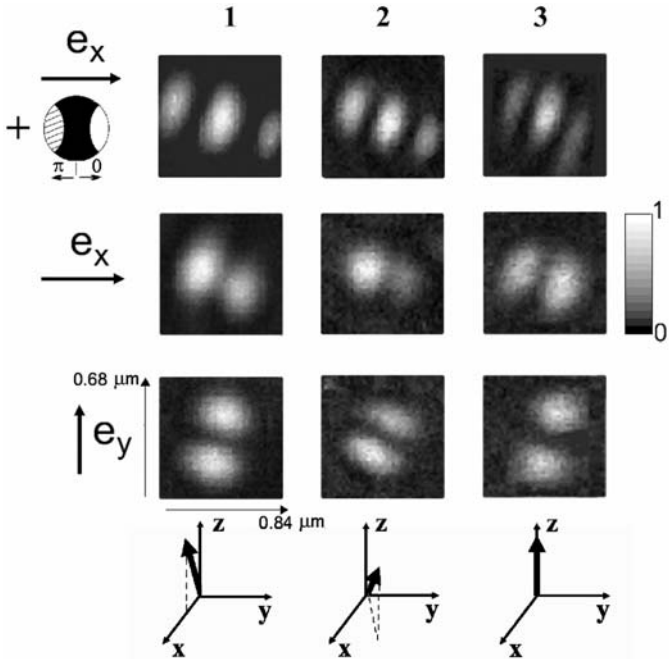

Fig. 5. Experimental fluorescence images of three out-of-plane different single molecules. Sample: sol-gel film doped with orange perylene molecules. Experimental images: molecule 1, 70×70 pixels, 10 ms/pixel, molecules 2 and 3, 40×40 pixels, 10 ms/pixel, $\lambda = 532$ nm, 100 μW. A constant background signal of 30 counts has been subtracted to the raw data. Real image size $= 0.84 \times 0.68$ μm^2 (see text, "experimental"). The linear intensity scale extends between 0 and 1. Each image is displayed with its maximum value equal to unity. Typical values of the maxima are 600 counts for the x-configuration of molecule 1, about 290 counts for the z-configuration and x-configuration of molecule 2 and 320 counts for the z-configuration of molecule 3. On left side, schematics of the polarisation configuration. For each line, from top to bottom: fluorescence pattern in the z-configuration with amplitude and phase masking, in the x-configuration without masking and initial polarisation along x, in the y-configuration without masking and a crossed polarisation. Bottom: approximative orientation of dipoles deduced from "visual" comparison with images 6 to 8.

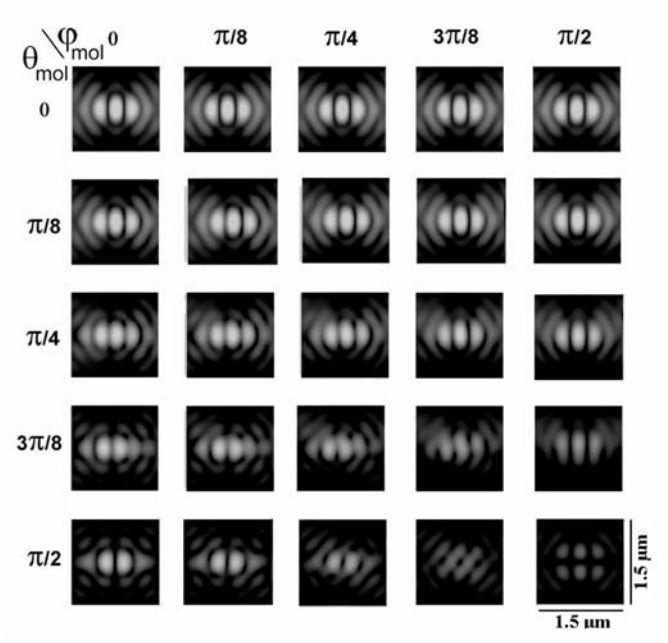

Fig. 6. Evolution of the calculated fluorescence patterns at the focal plane with respect with the dipole orientation. The figure corresponds to the z-configuration of polarisation. θ and φ are the polar angles of the dipole (see Fig. 4). Elementary image size $= 1.5 \times 1.5$ μm^2.

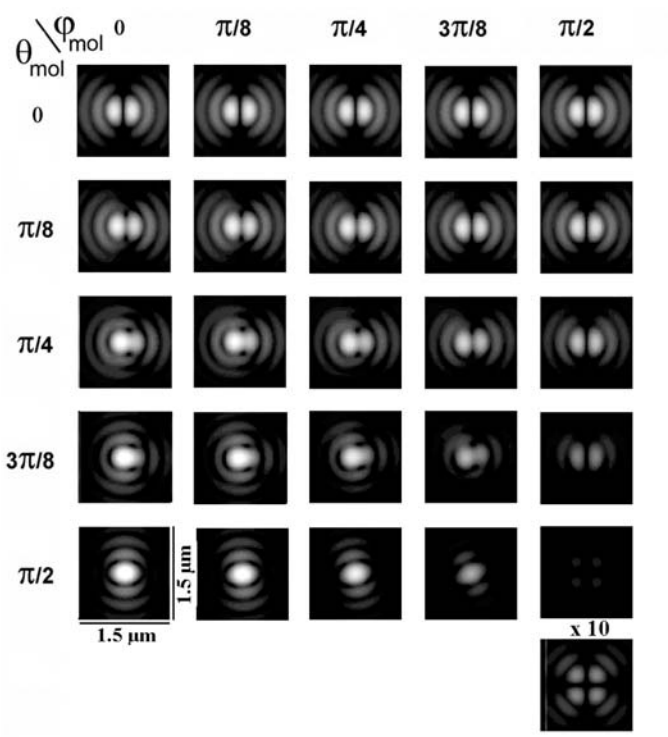

Fig. 7. Evolution of the calculated fluorescence patterns at the focal plane with respect with the dipole orientation. The figure corresponds to the x-configuration of polarisation. Same notations as in Figure 6. The additional pattern at bottom corresponds to the case $\theta_{\rm mol} = \pi/2$, $\varphi_{\rm mol} = \pi/2$ with a $\times 10$ magnification factor.

it is possible to derive from such images a quantitative value of the orientation of the dipole and furthermore to estimate the accuracy of this determination.

4 Quantitative determination of the dipole 3D orientation of single molecules

4.1 Procedure

In order to first derive a qualitative estimation of the dipole orientation of a given molecule, we have built a basis of calculated images, derived from the evaluation of equation (17), with a size of 1.5×1.5 μm^2. Examples of such images are displayed in Figures 6, 7 and 8 with $\theta_{\rm mol}$ and $\varphi_{\rm mol}$ varying from 0 to $\pi/2$ with a $\pi/8$ step.

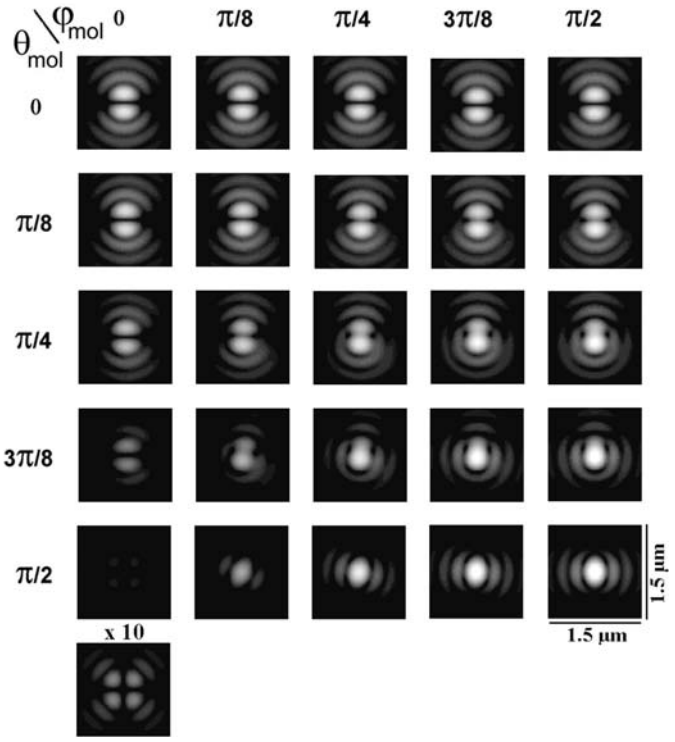

Fig. 8. Evolution of the calculated fluorescence patterns at the focal plane with respect with the dipole orientation. The figure corresponds to the y-configuration of polarisation. Same notations as in Figure 6. The additional pattern at bottom corresponds to the case $\theta_{\rm mol} = \pi/2$, $\varphi_{\rm mol} = 0$ with a $\times 10$ magnification factor.

As in the experimental procedure, three images are derived for a given dipole orientation, one for each of the polarisation configurations, in order to get a qualitative idea of the dipole orientation of a given molecule without any correlation procedure. Depending on this polarisation configuration, the expression of the field components, e'_x, e'_y and e'_z is given by equations (10) or (15). A quantitative comparison between the calculated set of images and the experimental one implies image correlation. This procedure allows us to optimise the correlation as a function of $\theta_{\rm mol}$ and $\varphi_{\rm mol}$. The optimum value of the image correlation maximum determines the angles $\theta^M_{\rm mol}$ and $\varphi^M_{\rm mol}$ of the dipole. The estimation of the accuracy of these values implies the calculation of the variations of the correlation maximum $C_M(\theta_{\rm mol}, \varphi_{\rm mol})$ as a function of $\theta_{\rm mol}$ with $\varphi_{\rm mol} = \varphi^M_{\rm mol}$ on one hand and as a function of $\varphi_{\rm mol}$ with $\theta_{\rm mol} = \theta^M_{\rm mol}$ on the other hand, on a limited range around the maxima $\theta^M_{\rm mol}$ and $\varphi^M_{\rm mol}$. The relevant curves are fitted by a polynomial function. The precision on the determination of $\theta^M_{\rm mol}$ and on $\varphi^M_{\rm mol}$ is obtained by calculating the following intervals:

$$\Delta\omega_{\rm mol} = \omega^1_{\rm mol} - \omega^2_{\rm mol}, \quad \text{with} \quad \omega_{\rm mol} = \theta_{\rm mol} \quad \text{or} \quad \varphi_{\rm mol}$$

such that,

$$C(\omega^M_{\rm mol}) - C(\omega^{1(2)}_{\rm mol}) \simeq N$$

where N is the standard deviation for the relevant polynomial fit, which gives an estimation of the correlation noise.

For each molecule, both the final value of the angles $\theta^M_{\rm mol}$ and $\varphi^M_{\rm mol}$ and the precision on these values are derived from the comparison of the three intervals obtained for the three different polarisation configurations. First $\theta^M_{\rm mol}$ and $\varphi^M_{\rm mol}$ must lie in each interval, except in some situations where one particular fit is meaningless. Indeed, some variations are not meaningful, for example when we analyse the images recorded in a polarisation configuration at 90° of the dipole orientation. In such a situation obviously, the fluorescence signal should be weak and the noise is high. The precision on the $\theta^M_{\rm mol}$ value (resp. $\varphi^M_{\rm mol}$) is typically the smallest calculated $\Delta\theta_{\rm mol}$ (resp. $\Delta\varphi_{\rm mol}$).

4.2 Results

The curves in Figure 9 show the variations of $C_M(\theta_{\rm mol}, \varphi_{\rm mol})$ with respect to $\theta_{\rm mol}$ then $\varphi_{\rm mol}$ for the molecule 1 (see Fig. 5). The fit step corresponds to 5°. The correlation process is derived from the raw experimental data except for the subtraction of a constant background, which is low compared to the maximum intensity of the images. The step of the two galvanometric mirrors cannot be independently controlled and we have measured, by using a calibrated grid, that the ratio between the elementary y-step and x-step is 0.8, whatever the value of the step is. The correlation process takes into account the tilt between the (x, y) frame of beam shaping and the (x, y) scan frame. The perfect matching of these two frames is difficult to control experimentally. It also accounts for the above-mentioned asymmetry of the laser scan in the two orthogonal directions. More specifically contrary to previous calculations (Figs. 2–3, 6–9), in this section, which is devoted to a quantitative comparison between experimental and calculated images, the images are calculated with a different step for the y- and x-directions, with a ratio equal to 0.8. The calculated image frame is moreover rotated in order to take into account the experimental tilt, which measured value is about 10°. The value of the maximum of correlation varies between 0.95 and 0.88 with respect to the polarisation configuration. In the case of the z-configuration, the correlation maximum is always slightly lowest than in the case of x- and y-configurations, but this correlation value remains indeed high. This can be readily explained by taking into account the small defects of the phase plate, the small experimental uncertainty on the position of the edge of the phase plate with respect to the beam and on the relative dimensions of the beam and of the mask. The experimental fluorescence pattern in this case is also more sensitive to the intensity homogeneity of the excitation beam. The high correlation values reflect the high signal to noise ratio obtained in the recording of single molecule fluorescence. The quantitative analysis of the curves (Fig. 9) demonstrates that $\theta^M_{\rm mol} = 0.5$ rad ($\Delta\theta^M_{\rm mol} = 0.1$ rad), i.e. 30° ($\Delta\theta^M_{\rm mol} = 6°$) and $\varphi^M_{\rm mol} = -0.053$ rad ($\Delta\varphi^M_{\rm mol} = 0.035$ rad), i.e. −3° ($\Delta\varphi^M_{\rm mol} = 2°$) for molecule 1. As a result the less precise fit corresponds to images recorded in the y-configuration since in this case the dipole is nearly at right angle to the

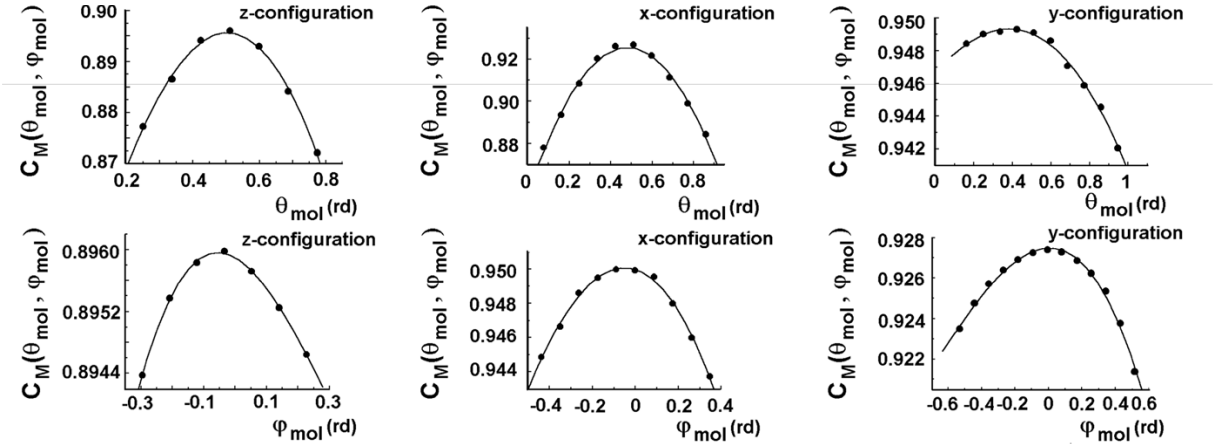

Fig. 9. Variations of the maximum of the image correlation value with respect to the single molecule dipole orientation. These curves are related to the molecule 1 (see Fig. 5). On the first line, variations of $C_M(\theta_{\rm mol}, \varphi_{\rm mol})$ with respect to $\theta_{\rm mol}$ in the three different configurations of polarisation. On the second line, idem for $\varphi_{\rm mol}$.

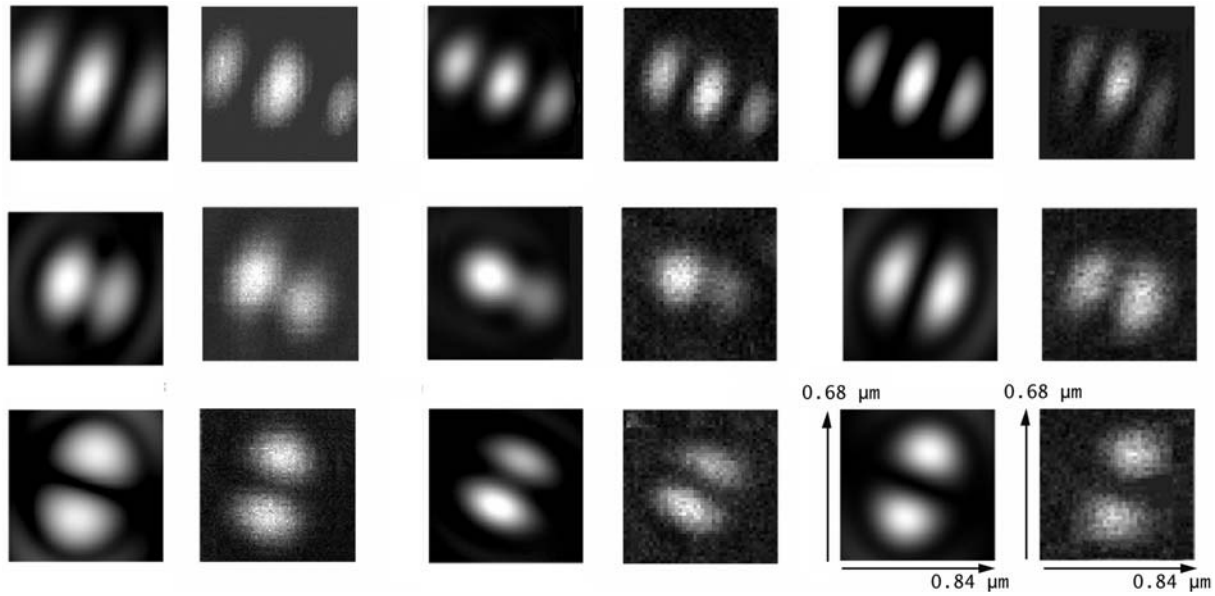

Fig. 10. Comparison between experimental and calculated fluorescence patterns. The square area of each displayed image corresponds to the raw recorded image. x and y real scales take into account the $y/x = 0.8$ experimental scan factor. First two columns: comparison for the molecule 1; second two columns: comparison for the molecule 2; third two columns: comparison for the molecule 3. As in other figures, from top to bottom, results for the z-configuration, the x-configuration and the y-configurations, respectively.

polarisation direction. This is in agreement with the dispersion observed on the relevant curves (Fig. 9). We have performed equivalent fits for molecules 2 and 3 (Fig. 5). In both cases, the values of the maximum correlation intensity are of the same order of magnitude as in the previous analysis. The values of $\theta^M_{\rm mol}$ and of $\varphi^M_{\rm mol}$ are 0.77 rad ($\Delta\theta^M_{\rm mol} = 0.1$ rad) and 0.45 rad ($\Delta\varphi^M_{\rm mol} = 0.04$ rad), i.e. 44° (6°) and 26° (2°) for molecule 2 and 0.09 rad ($\Delta\theta^M_{\rm mol} = 0.09$ rad) and 3.28 rad ($\Delta\varphi^M_{\rm mol} = 0.11$ rad), i.e. 5° (5°) and 188° (7°) for molecule 3. For these two molecules, the best precision on the value of the angle $\theta^M_{\rm mol}$ is obtained from the analysis of the image in the z-configuration. It is in agreement with the fact that the weight of the z-component of the dipole is high for both of them. If so, the analysis of the image recorded in the z-configuration has an increasing importance and allows one to determine the tilt of the dipole $\theta^M_{\rm mol}$ with precision. This analysis demonstrates that the dipole orientation is determined with a precision that is better than 10° with this simple polarisation set-up. It also appears that it is often sufficient to record two images to derive a good estimation of the dipole orientation. Nevertheless, the suitable set of images varies with the dipole orientation. When the dipole of the molecule has an out-of-plane component, the z-configuration image is needed, whereas when this component is very weak, only the images in the x- and y-configurations are important. Among the three reported molecules, one is right off-plane, one is at 45° of the sample plane and the last one is at 30° from the plane. The accuracy of the determination of the orientation of

the dipoles demonstrates that the simple implemented polarisation set-up is very efficient to excite and to detect molecules whatever their dipole orientation. Inversely, the high signal-to-noise ratio obtained in the detection of single molecules allows us to use the fluorescence signal as a map of the excitation field pattern in the focus plane. In particular in the case of molecule 3 which dipole is perpendicular to the sample plane, the fluorescence pattern reproduces the pattern of the z-component of the field. The very good agreement obtained between the calculated patterns and the experimental ones demonstrates that the above model satisfyingly describes the field obtained after a high-numerical aperture and after crossing an interface. Finally, the comparison between the experimental data and the calculated images is displayed in Figure 10.

5 Conclusion

By combining amplitude and phase masking, we obtain a large component of the field that is polarised along the axis of a microscope. Such a configuration can be used to excite off-plane molecules. Furthermore a configuration involving phase masking can be compatible with confocal microscopy. As a result the SNR in the detection of the fluorescence of an off-plane oriented single molecule can be high. We have explicitly calculated the fluorescence patterns that should be observed at the focal plane, after an interface for particular amplitude and phase masks. The calculations, which rely on the principle that free propagation is exactly described in the frame of plane-wave decomposition, can be readily applied to different masks. The calculated fluorescence patterns have been quantitatively compared to experimental images of single molecules by the way of an image correlation algorithm. The agreement between experimental images and calculated ones is satisfying. It demonstrates that the model is well suited to describe the polarisation configuration when the beam is focussed by a high-numerical objective at the focal plane above the substrate interface. This procedure allowed us to determine the 3D dipolar orientation of different off-plane molecules, with a direction accuracy that is better than 10° for both polar angles.

References

1. *Single Molecule Optical Detection, Imaging and Spectroscopy*, edited by T. Basché, W.E. Moerner, M. Orrit, U.P. Wild (VCH, Weinheim, 1997)
2. N.-F. van Hulst, J.-A. Veerman, M.F. García-Parajó, L. Kuipers, J. Chem. Phys. **112**, 7799 (2000)
3. S. Weiss, Science **283**, 1676 (1999)
4. F. Güttler, M. Croci, A. Renn, U.P. Wild, Chem. Phys. **211**, 421 (1996)
5. J.J. Macklin, J.K. Trautman, T.D. Harris, L.E. Brus, Science **272**, 255 (1996)
6. L. Novotny, E.J. Sanchez, X.S. Xie, Ultramicroscopy **71**, 21 (1998)
7. J. Azoulay, A. Débarre, A. Richard, P. Tchénio, Europhys. Lett. **51**, 374 (2000)
8. L. Novotny, E.J. Sanchez, X.S. Xie, Phys. Rev. Lett. **82**, 4014 (1999)
9. J. Azoulay, A. Débarre, P. Tchénio, J. Microscopy **194**, 486 (1999).
10. E. Betzig, R.J. Chichester, Science **262**, 1422 (1993)
11. J.A. Veerman, M.F. Garcia-Parajo, L. Kuipers, N.F. Van-Hulst, J. Microscopy **194**, 477 (1999)
12. J. Jasny, J. Sepiol, Chem. Phys. Lett. **273**, 297 (1997)
13. S.A. Empodocles, R. Neuhauser, M.G. Bawendi, Nature **399**, 126 (1999)
14. A.P. Bartko, R.M. Dickson, J. Phys. Chem. B **103**, 11237 (1999)
15. B. Sick, B. Hecht, L. Novotny, Phys. Rev. Lett. **85**, 4482 (2000)
16. M. Vacha, M. Kotani, J. Chem. Phys. **118**, 5279 (2003)
17. J. Enderlein, Chem. Phys. Lett. **308**, 263 (1999)
18. J.T. Fourkas, Opt. Lett. **26**, 211 (2001)
19. J. Azoulay, A. Débarre, R. Jaffiol, P. Tchénio, Single Mol. **2**, 241 (2001)
20. L. Novotny, M.R. Beversluis, K.S. Youngworth, T.G. Brown, Phys. Rev. Lett. **86**, 5251 (2001)
21. N. Huse, A. Schonle, S.W. Hell, J. Biomed. Opt. **6**, 480 (2001)
22. E. Wolf, Proc. R. Soc. Lond. A **253**, 349 (1959); J.T. Fourkas, Opt. Lett. **26**, 211 (2001)
23. J. Gasper, G.C. Sherman, J. Stamnes, J. Opt. Soc. Am. **66**, 955 (1976)
24. P. Török, P. Varga, G.R. Booker, J. Opt. Soc. Am. **12**, 2136 (1995)